Coupling Two Ultra-high-Speed Cameras to Elucidate Ultrasound Contrast-Mediated Imaging and Therapy

Li, Hongchen; Li, Xiufeng; Collado-Lara, Gonzalo; Lattwein, Kirby R.; Mastik, Frits; Beurskens, Robert; van der Steen, Antonius F.W.; Verweij, Martin D.; de Jong, Nico; Kooiman, Klazina

DOI
10.1016/j.ultrasmedbio.2022.08.020

Publication date
2023

Document Version
Final published version

Published in
Ultrasound in Medicine and Biology

Citation (APA)
Li, H., Li, X., Collado-Lara, G., Lattwein, K. R., Mastik, F., Beurskens, R., van der Steen, A. F. W., Verweij, M. D., de Jong, N., & Kooiman, K. (2023). Coupling Two Ultra-high-Speed Cameras to Elucidate Ultrasound Contrast-Mediated Imaging and Therapy. *Ultrasound in Medicine and Biology*, *49*(1), 388-397. https://doi.org/10.1016/j.ultrasmedbio.2022.08.020

Ultrasound in Med. & Biol., Vol. 49, No. 1, pp. 388–397, 2023

0301-5629/$ - see front matter

https://doi.org/10.1016/j.ultrasmedbio.2022.08.020

● *Technical Note*

COUPLING TWO ULTRA-HIGH-SPEED CAMERAS TO ELUCIDATE ULTRASOUND CONTRAST-MEDIATED IMAGING AND THERAPY

Hongchen Li,* Xiufeng Li,† Gonzalo Collado-Lara,* Kirby R. Lattwein,* Frits Mastik,* Robert Beurskens,* Antonius F.W. van der Steen,*,† Martin D. Verweij,*,† Nico de Jong,*,† and Klazina Kooiman*

* Department of Biomedical Engineering, Thoraxcenter, Erasmus MC University Medical Center Rotterdam, Rotterdam, The Netherlands; and † Section of Medical Imaging, Department of Imaging Physics, Delft University of Technology, Delft, The Netherlands

(*Received* 5 *April* 2022; *revised* 26 *August* 2022; *in final form* 31 *August* 2022)

Abstract—Ultrasound contrast-mediated medical imaging and therapy both rely on the dynamics of micron- and nanometer-sized ultrasound cavitation nuclei, such as phospholipid-coated microbubbles and phase-change droplets. Ultrasound cavitation nuclei respond non-linearly to ultrasound on a nanosecond time scale that necessitates the use of ultra-high-speed imaging to fully visualize these dynamics in detail. In this study, we developed an ultra-high-speed optical imaging system that can record up to 20 million frames per second (Mfps) by coupling two small-sized, commercially available, 10-Mfps cameras. The timing and reliability of the interleaved cameras needed to achieve 20 Mfps was validated using two synchronized light-emitting diode strobe lights. Once verified, ultrasound-activated microbubble responses were recorded and analyzed. A unique characteristic of this coupled system is its ability to be reconfigured to provide orthogonal observations at 10 Mfps. Acoustic droplet vaporization was imaged from two orthogonal views, by which the 3-D dynamics of the phase transition could be visualized. This optical imaging system provides the temporal resolution and experimental flexibility needed to further elucidate the dynamics of ultrasound cavitation nuclei to potentiate the clinical translation of ultrasound-mediated imaging and therapy developments. (E-mail: h.li@erasmusmc.nl) **© 2022 The Author(s). Published by Elsevier Inc. on behalf of World Federation for Ultrasound in Medicine & Biology. This is an open access article under the CC BY-NC-ND license (http://creativecommons.org/licenses/by-nc-nd/4.0/).**

Key Words: **Cavitation, Droplet, Microbubble, Ultra-high-speed imaging, Ultrasound, Ultrasound contrast agents.**

INTRODUCTION

Ultrasound contrast-mediated imaging and therapy, which use ultrasound contrast agents (UCAs) for a more enhanced and/or disease-targeted approach to diagnosis and treatment, have seen rapid development over the last 15 years (Christensen-Jeffries et al. 2020; Kooiman et al. 2020; Deprez et al. 2021). UCAs such as lipid-coated gas microbubbles and polymer-shelled droplets respond to ultrasound through oscillation and vaporization, respectively, which can provide high contrast from linear tissue echoes and induce microstreaming, shear stress, microjets and other impacts on cells or tissues (Helfield 2019; Kee and Teo 2019). Ultra-high-speed optical imaging observations of ultrasound-activated microbubbles have helped us to understand their dynamics (Bloch et al. 2004; Thoroddsen et al. 2008; Mulvana et al. 2017), resonance frequency (Sun et al. 2005; Sijl et al. 2008), shape oscillation (Versluis et al. 2010; Hay et al. 2013; Liu et al. 2018), clustering (Kokhuis et al. 2011; Lazarus et al. 2017) and the influence of microbubble composition and lipid handling on the acoustic response (Segers et al. 2018a; Langeveld et al. 2021). Additionally, ultra-high-speed imaging has also been instrumental in understanding the mechanisms underlying acoustic droplet vaporization (ADV) (Shpak et al. 2014; Zhou 2015; Wu et al. 2021). These phase shift droplets have exhibited functionality in drug delivery (Sirsi and Borden 2014; Lee et al. 2017; Song et al. 2021), tumor characterization and treatment (Rapoport et al. 2011; Sheng et al. 2021),and proton therapy (Carlier et al. 2020; Collado-Lara et al. 2022). When UCAs

Address correspondence to: Hongchen Li, Office Ee2302, PO Box 2040, 3000 CA Rotterdam, The Netherlands. E-mail: h.li@erasmusmc.nl

are restricted by a boundary, as in the vascular system, asymmetric phenomena such as microbubble non-spherical oscillations (Dollet et al. 2008; Vos et al. 2011; Guedra et al. 2016), microbubble rupture and jet formation during microbubble collapse (Chen et al. 2011a, 2011b; Lajoinie et al. 2018; Cleve et al. 2019; Zevnik and Dular 2020) and prolonged ADV (Cho and Son 2018a, 2018b) can arise upon ultrasound activation. In the aim of understanding the interaction between UCAs and cells (mammalian and bacterial), ultra-high-speed recordings have led to important insights into such phenomena as sonoporation (Prentice et al. 2005; Fan et al. 2014a, 2014b; Helfield et al. 2016), intercellular junction opening (Beekers et al. 2020) and biofilm elimination (Goh et al. 2015; Kouijzer et al. 2021). These insights support and aid in the development and clinical translation of UCAs-mediated therapeutic applications.

Performance and adaptability constraints, such as frame rate, recording duration and resolution, are always present in ultra-high-speed imaging systems, and the application dictates which constraints exist and to what extent. Imaging configurations to optimally suit a specific application are often determined by experimental and financial limitations. Research related to the use of UCAs for imaging and therapy requires an advanced ultra-high-speed optical imaging system that is able to accomplish sufficient temporal and spatial resolution (Gelderblom et al. 2012; Versluis 2013). However, in practice, a trade-off exists between recording speed and recording duration for any practical application. An ultra-high-speed system up to 200 million frames per second (Mfps) can only record 24 frames maximally, while other ultra-high-speed systems can record hundreds of microseconds but the recording speed has a maximum of 1 Mfps with limited resolution (Chen et al. 2013; Xing et al. 2017).

To observe phenomena with clinically used ultrasound frequencies ($\leq$10 MHz), an ultra-high-speed imaging system with a frame rate of at least 20 Mfps is needed. Existing custom-made ultra-high-speed systems have been used to investigate the dynamic behaviors of UCAs, including the Brandaris 128 (Chin et al. 2003) and UPMC Cam (Chen et al. 2013), which are both capable of recording 128 frames with a frame rate up to 25 Mfps, and the Ultranac, which is capable of recording microbubble oscillation up to 20 Mfps but with only 24 consecutive images (Kudo 2017). These ultra-high-speed optical imaging systems have provided a better understanding of UCAs oscillation phenomena. However, such custom-made systems are costly in construction and maintenance, not commercially available and can lack flexibility because of the very large and heavy spatial design. New relevant challenges are lacking investigations because of the limitations of the current systems, such as having a complex operation that is user-unfriendly, inconvenient data transfer and costly maintenance. Thus, a new and easier-to-control system should be proposed that is capable of addressing the anticipated scientific questions for the coming decade.

To date, it is still challenging to observe UCAs' oscillation or phase shift in different cross-sectional planes at an extremely high speed ($\geq$10 Mfps) and long duration ($>$10 μs) with an operationally flexible ultra-high-speed imaging solution. This limits the further discovery of the physical, chemical and biological mechanisms of ultrasound-mediated imaging and treatment and the related optimization to achieve optimal results. In addition, different optical view angles can provide a thorough understanding of the dynamic UCA oscillations in three dimensions (Vos et al. 2011). To overcome these technological challenges, we developed a novel ultra-high-speed imaging system by coupling two small-sized, commercially available, user-friendly 10-Mfps cameras. The coupling was set up with the two cameras recording in either the same plane, increasing the effective acquisition frame rate to 20 Mfps, or in orthogonal planes, for example, allowing visualization of the 3-D dynamics of the phase transition. Two verification experiments were performed for the 20-Mfps interleaved recording and one experiment for the orthogonal observation at 10 Mfps.

METHODS

Two camera coupling for 20-Mfps imaging

The highest recording speed of a single HPV-X2 ultra-high-speed camera (Shimadzu Corp., Kyoto, Japan) is 10 Mfps with an exposure time of 50 ns and duration of 25.6 μs, capturing 256 frames. This camera uses a FTCMOS2 image sensor (Kuroda et al. 2016) which has 400 $\times$ 250 pixels (FP mode) with 10-bit gray-scale values; the pixel size is 32 $\times$ 32 μm. This ultra-high-speed modality has been applied to fuel engineering (Ding et al. 2016), materials mechanical testing (Dave et al. 2018; Koch et al. 2021) and the biomedical field (Cleve et al. 2019; Morton et al. 2021; Wu et al. 2021). While this camera records at 10 Mfps, its 50-ns exposure time makes it possible to interleave the two cameras to achieve a 20-Mfps recording speed. To accomplish this, two cameras were electronically coupled with a 5-m high-speed network cable (S/FTP, Cat 6, Goobay, The Netherlands) using their internal synchronization function. Each camera was controlled with a separate computer, both installed with the same controlling software (Shimadzu Corp., Kyoto, Japan). Hence, by setting different delay times in each of the two controlling programs with a minimum step of 10 ns, different recording modes could be achieved. For example, the 20-Mfps

recording speed was achieved by setting a 50-ns delay between the two cameras that were separately working at 10 Mfps.

To verify the 20-Mfps recording speed, first a strobe LED flashing experiment was implemented with the setup shown in Figure 1. For the coupling, the two cameras were labeled camera 1 and camera 2, with camera 1 aimed to record 50 ns earlier than camera 2. Two synchronized high-frequency strobe LED lights (L-7113GC, 5 mm, Green, Kingbright Electronic Co, Ltd, Taipei, Taiwan) were separately placed toward the two cameras to which macrolenses (Tamron 60-mm F/2.0 Macro SP Di II, Köln, Germany) were connected. The two LEDs were driven by a dual non-inverting metal−oxide−semiconductor field-effect transistor (MOSFET) driver circuit (IXDN602, IXYS, Leiden, The Netherlands) at 6.67 MHz and 1/3 on/off duty cycle (50 ns on and 100 ns off) for 160 pulses. The output of the LED was measured by a fast-response photodiode (SM05PD2B Mounted Silicon Photodiode, 200−1100 nm, Anode Grounded, Thorlabs, Germany), to ensure an accurate on/off duty cycle (50 ns on and 100 ns off; see Fig. S1, online only). Both the signal generator (WW2572A, Tabor Electronics, San Francisco, CA, USA) for the LED driver and camera 1 were triggered by the same arbitrary waveform generator (AWG; DG1022Z, RIGOL Technologies, Munich, Germany), while the start of the LEDs was delayed 1450 ns based on the 850-ns initialization time of each camera, aimed to obtain dissimilar on−off state patterns from two cameras. The two "AUX" output ports from the two cameras were connected to an oscilloscope (HMO1002, Rohde & Schwarz, Munich, Germany) using two identical Bayonet Neill−Concelman (BNC) cables (Coaxial Cable Assembly, RG58, Farnell, Utrecht, The Netherlands) to confirm the delay time between the two cameras according to their exposure timings.

The second 20-Mfps interleaved recording experiment focused on ultrasound-activated microbubble oscillations. To visualize the microbubble oscillation on ultrasound insonification, the two-camera system was air-coupled to two output ports of an Olympus bright-field microscope (BXFM, Olympus Optical, Japan) at 60 × objective (LUMPLFLN60XW, Olympus Optical, Japan) (see Fig. 2a). The acquisitions from the two cameras were first registered by using affine transformations to correct for small misalignments (Chin et al. 2003). DSPC (1,2-distearoyl-*sn*-glycero-3-phosphocholine)-based lipid-coated microbubbles with a C_4F_{10} gas core were made using the indirect method by probe sonication as described previously (Langeveld et al. 2021). Microbubbles were placed into a phosphate-buffered saline-filled IbiTreat polymer μ-Slide (80196; 0.8 mm channel height; I Luer; Ibidi GmbH, Grafelfing, Germany) at a concentration of 5×10^5 mL^{-1} at room temperature. A single-element transducer (76.2-mm focal length, 2.25-MHz center frequency, −6-dB beam width of 3 mm at 2

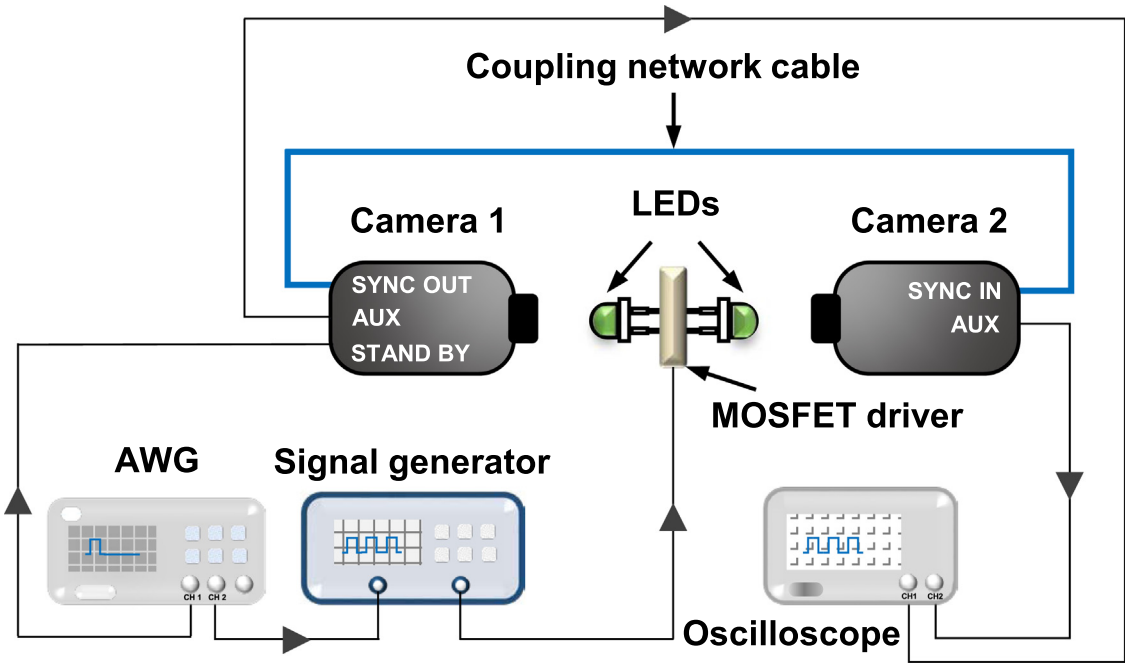

Fig. 1. Validation setup of the two ultrahigh-speed cameras interleaved to achieve 20-Mfps recording using two strobe LEDs (not drawn to scale). AWG = arbitrary waveform generator; LEDs = light-emitting diodes.

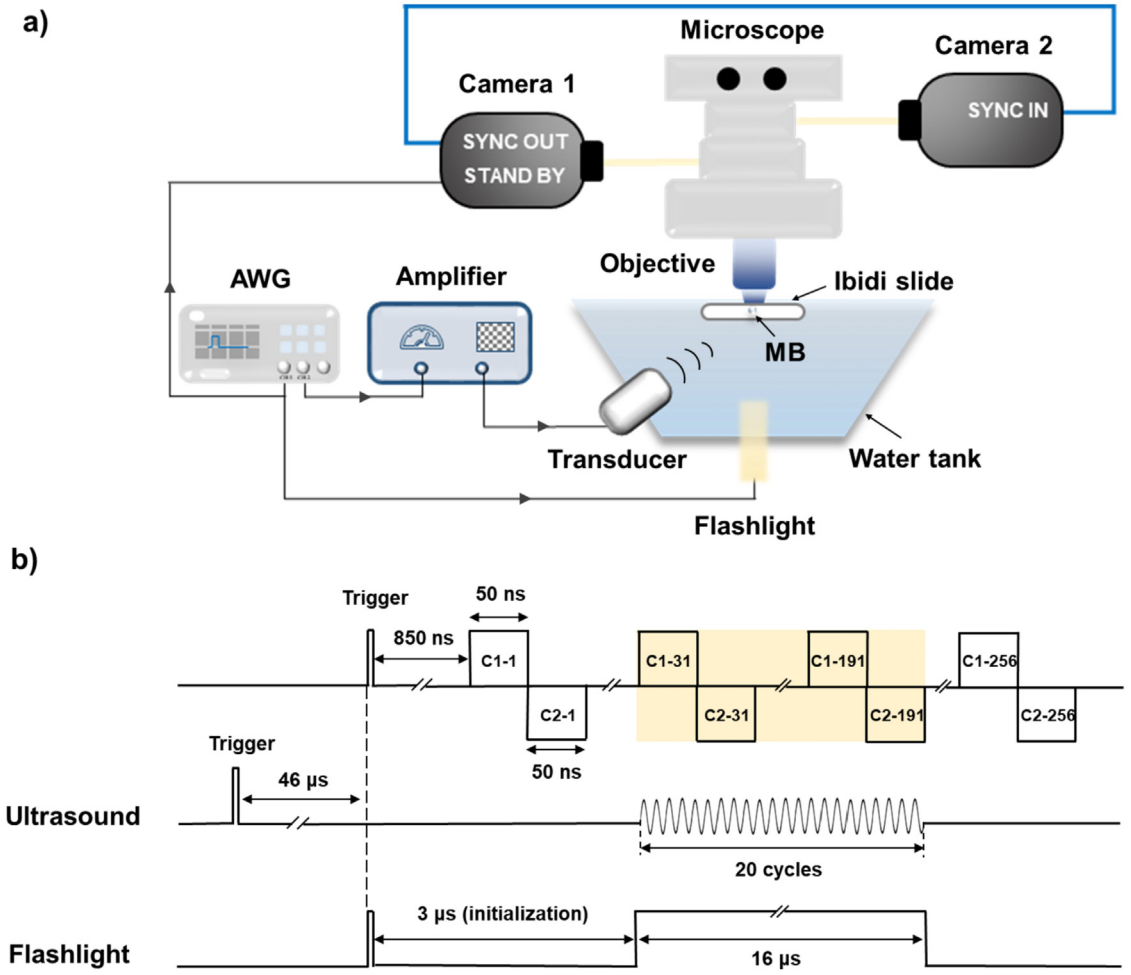

Fig. 2. Experimental setup for 20-Mfps interleaved recording of microbubble oscillation. (a) Schematic of the setup (not drawn to scale). (b) Corresponding experimental timelines. C1 and C2 represent camera 1 and camera 2, respectively, and are followed by the frame number. The *yellow box* indicates when the light source was on during the camera recordings. AWG = arbitrary waveform generator; MB = microbubble; MOSFET = metal−oxide−semiconductor field-effect transistor.

MHz; V305, Panametrics-NDT, Olympus, Waltham, MA, USA) was placed underneath the μ-Slide at a 45° angle to insonify the microbubbles. An AWG (33220A, Agilent, Santa Clara, CA, USA) in combination with a broadband amplifier (ENI A-500, Electronics & Innovation, Rochester, NY, USA) was connected to the transducer. The transducer output was calibrated using a needle hydrophone (1-mm diameter; PA2293, Precision Acoustics, Dorchester, UK) and the ultrasound was applied as a 2-MHz, 100-kPa peak negative pressure, single 20-cycle burst. To account for the ultrasound propagation time, the two-camera system and the flashlight (MVS-7010, PerkinElmer, Waltham, MA, USA) were delayed 46 μs after the ultrasound was sent (shown in Fig. 2b). After acquisition of the microbubble oscillation recordings, the microbubble oscillating radius was tracked from each recording using the Hough transform and interpolated using the Piecewise Cubic Hermite Interpolating Polynomial (PCHIP) when plotting in MATLAB (The MathWorks, Natick, MA, USA). An intensity normalization was applied before the Hough transform because of the unequal amounts of light that each camera recorded.

Two-camera coupling for orthogonal imaging

To illustrate the flexibility of the two-camera coupled system, the cameras were installed in a configuration that allowed for the simultaneous recording of two orthogonal views (*i.e.,* top and side views). The top view was recorded by one 10-Mfps camera that was air-coupled to a bright-field microscope (BXFM, Olympus Optical, Japan) using a 40 × objective (LUMPLFLN40XW, working distance = 3.3 mm, Olympus Optical, Japan). The side view was recorded by the other 10-Mfps camera coupled

to a microscope-like optical path that combined an identical 40 × objective and corresponding tube lens (f200, convex, Spindler und Hoyer GmbH, Göttingen, Germany) (see Fig. 3a). The objectives were previously modified to avoid physical contact with each other as described in detail by Vos et al. (2011). The side view objective was held by a custom-made three-axis stage, and the tube lens was mounted on the back side of the objective.

The concept was validated with the simultaneous recording of ADV from the two orthogonal views. Droplets with a C_4F_{10} core and a cross-linked polymeric shell made of polyvinyl alcohol (Collado-Lara et al. 2022) were used. The droplets were suspended in a water-filled container made from an acoustically and optically transparent polycarbonate membrane, where they sunk to the bottom surface because of the higher density of the droplet compared with water. ADV was triggered with a 7.5-MHz single-element transducer (12.7-mm focal length, 7.5-MHz center frequency, −6-dB bandwidth 75%; V320, Panametrics-NDT), placed underneath the container at a 45° angle. The transducer was driven by an AWG (DG1022Z, RIGOL Technologies), in combination with an amplifier (68 dB, 150A-100B, Amplifier Research, EMV Benelux B.V., The Netherlands). A single 4-cycle pulse with a center frequency of 7.5 MHz was set with a 5.2-MPa peak negative pressure, as calibrated with a 1-mm-diameter hydrophone (PA2293, Precision Acoustics, Dorchester, UK), which is above the expected ADV threshold to ensure vaporization. To account for the ultrasound propagation time, the two

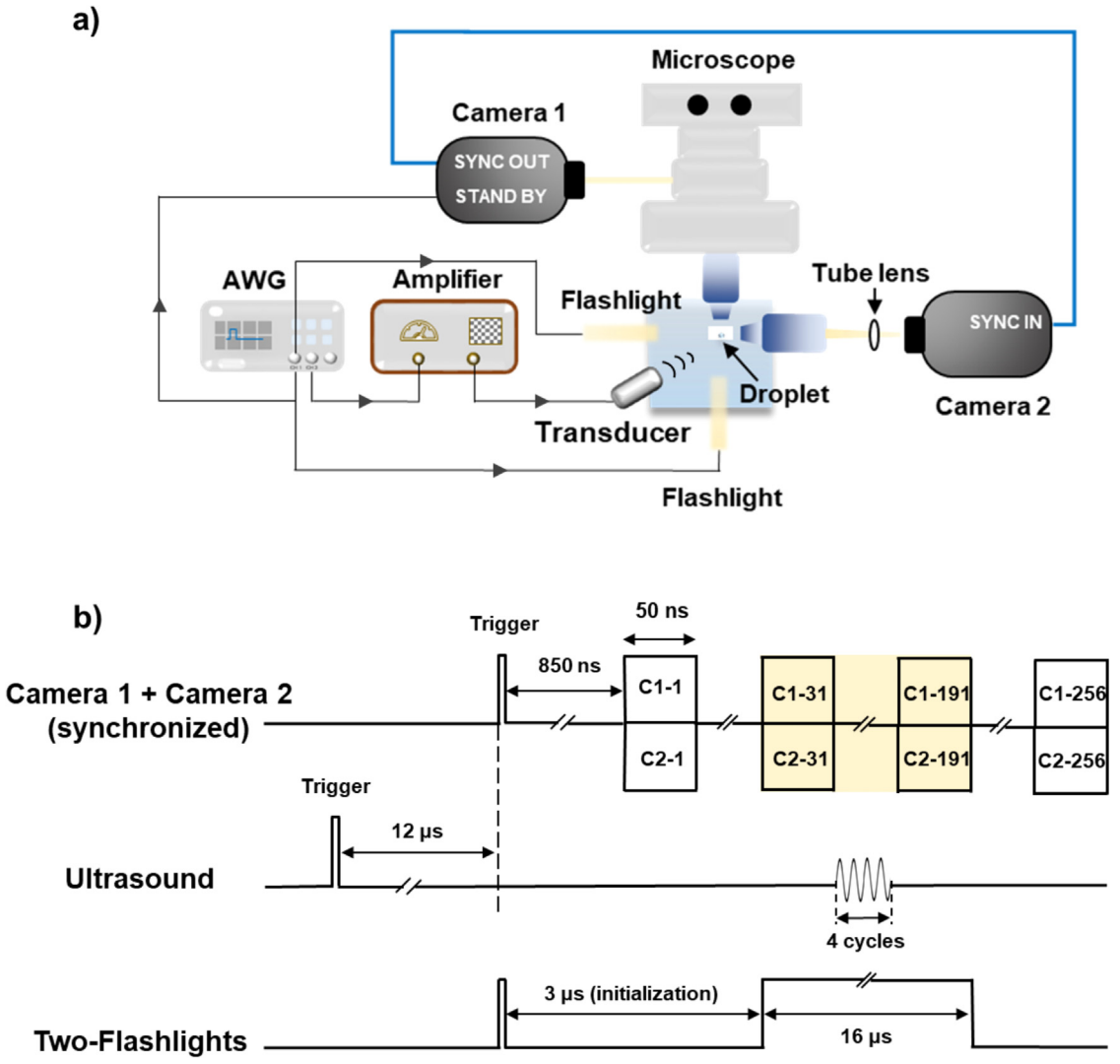

Fig. 3. Experimental setup for the orthogonal observation of acoustic droplet vaporization at 10 Mfps. (a) Schematic of the setup (not drawn to scale). (b) Corresponding experimental timelines. C1 and C2 represent camera 1 and camera 2, respectively, and are followed by the frame number. The *yellow box* indicates when the light source was on during the camera recordings. AWG = arbitrary waveform generator.

cameras and two flashlights (MVS-7010, PerkinElmer) were delayed 12 μs after the transducer was excited (see Fig. 3b). No time delay was set between the two cameras in the aim of recording simultaneously at 10 Mfps from two views.

RESULTS

Two-camera coupling for 20-Mfps imaging

Each camera recorded 256 frames, so 512 frames in total were recorded for the 2-camera coupled system, resulting in a full recording duration of 25.65 μs in the interleaved mode. Figure 4a and Video S1 (online only) illustrate the timing of the LEDs and the two-camera system, where the selected frames were integrated. The results indicate that the two cameras acquired unique intensity patterns of the flashing LEDs at different time points. Camera 1 exhibited a repeated pattern of bright, dark, dark, whereas camera 2 exhibited a repeated pattern of dark, bright, dark during the complete 160-LED-driven flashes. The patterns indicate that the two cameras captured the "on" status of the LED in an interleaved way, thereby verifying that the exposure delay (50 ns) between the two cameras was accurately controlled.

Figure 4b illustrates the output signals from the two cameras that indicate the exposure timing of each recorded frame, where an interleaved signal with two colors was easily found in the zoomed-in figure. To accurately investigate the timing shift, the two output signals were further processed by calculating the cross-correlation, which resulted in a time delay of 48.6 $\pm$ 0.05 ns between the two signals, as illustrated in Figure 4c, which is 2.8% less than the required 50 ns. To further validate the repeatability of the interleaving time, 10 different runs on 3 separate days (30 runs in total) were tested and cross-correlated. The results reveal that 23 runs had the same interleaving time of 48.6 $\pm$ 0.05 ns, while three runs had 48.5 $\pm$ 0.05 ns and four runs had 48.3 $\pm$ 0.05 ns, which is less than a 0.6% variation in interleaving time.

In Figure 5a are a selection of full-size (83.5 $\times$ 52.2 μm) and cropped frames of a vibrating microbubble captured by the two-camera system (see the interleaved video in Video S2, online only). The extracted

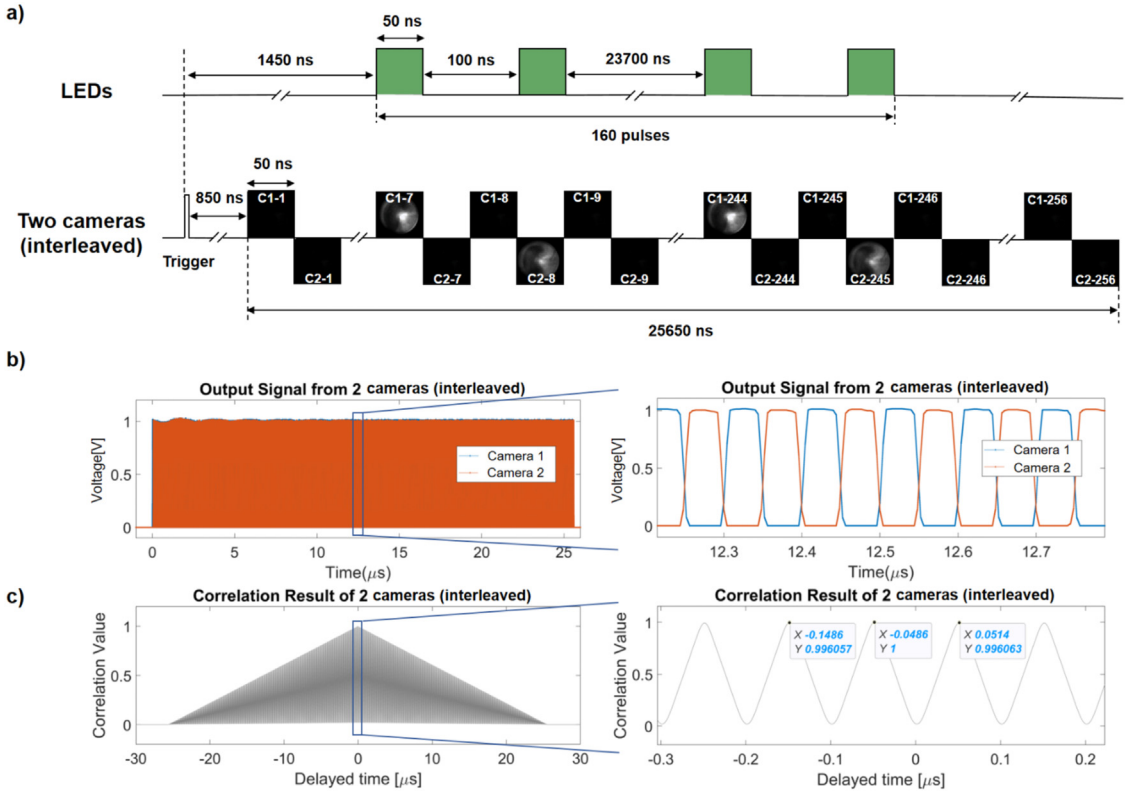

Fig. 4. 20 Mfps interleaved imaging results of strobe LEDs. (a) The timelines of the LEDs and the two cameras with selected frames of recorded flashing LEDs. Each green box represents when the LEDs were emitting during the interleaved imaging of the two cameras. C1 and C2 represent camera 1 and camera 2, respectively, and the number after the dash is the frame number. See the complete recording in Video S1 (online only). (b) Output signals of the exposure timing of each recorded frame from two cameras (c) Cross-correlation of the two signals of exposure timing. LEDs = light-emitting diodes.

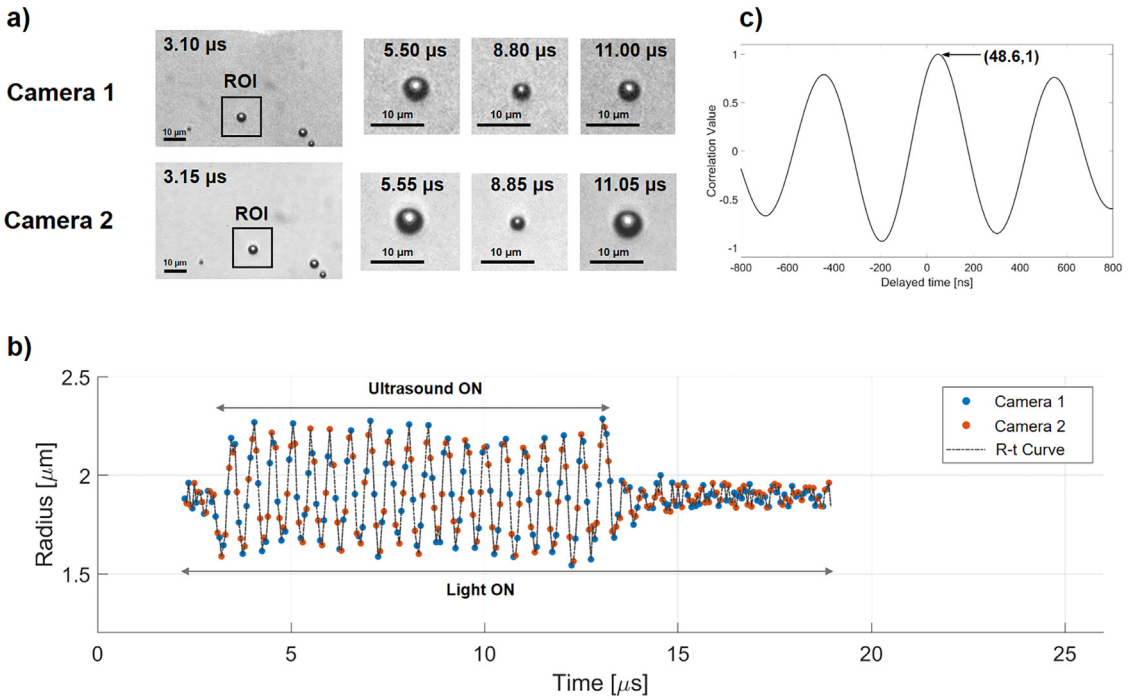

Fig. 5. Twenty-million-frame-per-second interleaved imaging results of the microbubble oscillation. (a) Selected frames from the interleaved imaging of two cameras. In the first row of images are the original images from two cameras (83.5 × 52.2 μm) with the region of interest (ROI) selected for the subsequent frames. See the complete recording in Video S2 (online only). (b) Temporal evolution of tracked microbubble oscillation visualizing the radius as a function of time. (c) The cross-correlation between two radius−time curves.

radius−time curve indicates that the microbubble had a resting radius of 1.8 μm and oscillated for 20 cycles, and that there was a time delay between the two cameras (Fig. 5b). To accurately investigate the time delay, the radius−time data were further processed by calculating the cross-correlation between two radius−time curves after removing their mean value separately, which resulted in a time delay of 48.6 ± 0.05 ns between the two cameras, as illustrated in Figure 5c. This time delay matches the result from the output signal mentioned above, and is 2.8% less than the 50-ns exposure time.

Two-camera coupling for orthogonal imaging

In Figure 6 are the selected frames of an example of the acoustic vaporization of a droplet with an initial diameter of 6.0 μm (3.6 μs, top view) recorded by the two-camera system. The acoustically induced phase transition started at 3.8 μs, marked by a small gas−liquid interface, which was captured from the top view. The interface is more visibly apparent in Video S3 (online only). The process continued with an expansion of the vaporized bubble until 15.2 μs, when the induced microbubble reached its maximum diameter (37.2 μm, top view) and then started to shrink. From the top view, the vaporization process was symmetric, whereas from the side view it was obvious that the vaporized bubble expanded asymmetrically, resulting in a dome shape, which indicates a smaller (roughly half) volume than a complete sphere.

DISCUSSION

This ultra-high-speed imaging system consisting of two coupled, commercially available cameras achieves the sub-micrometer spatial resolution and up to 50-ns temporal resolution that make it possible to study ultrasound-activated microbubble oscillation and droplet vaporization. This system offers high flexibility, which was translated into two different configurations that were used in the work described here. In the first, both cameras recorded the same plane in an interleaved manner, achieving 20 Mfps, which was repeatable and stable under the current coupling approach. The frame rate was verified by on−off state patterns acquired from two cameras using two strobe LEDs and by the recording of single microbubble oscillations. In the second configuration, the cameras recorded simultaneously the same object from two orthogonal views. This allowed observation of the phase transition of a superheated droplet near a boundary and its subsequent asymmetric oscillations, from the side view at 10-Mfps recording speed.

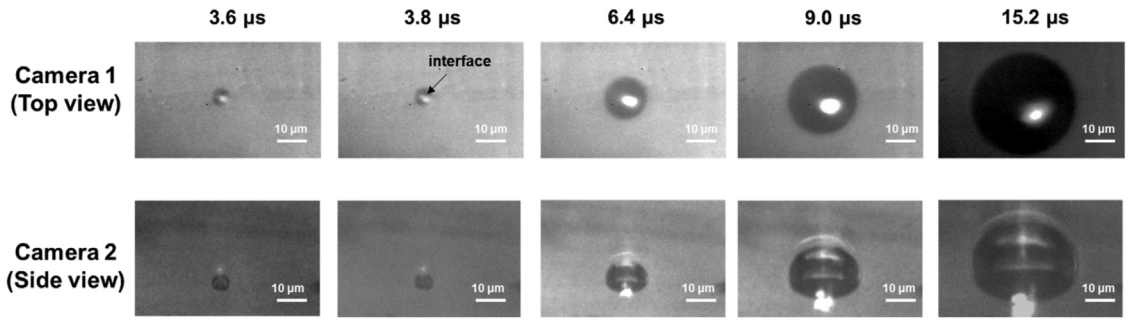

Fig. 6. Selected frames from the two cameras on the orthogonal observation of acoustic droplet vaporization at 10-Mfps recording speed. The complete recording can be found in Video S3 (online only). Bar = 10 μm in all images.

Ultrasound-activated microbubble oscillation (Fig. 5) was monitored with the two-camera system at 20 Mfps when ultrasound was applied at a clinically relevant frequency (2 MHz). The two-camera system achieved a 19.2 μs longer recording duration compared with other ultra-high-speed cameras at 20 Mfps (Faez et al. 2012; Chen et al. 2013). With a longer recording duration, it will be possible to record microbubble clustering and coalescence phenomena, which were difficult to achieve for other ultra-high-speed systems such as the Brandaris 128 (Beekers et al. 2019). This feature can contribute to the exploration of the underlying mechanisms of microbubble-mediated biofilm elimination and enhanced drug-delivery efficiency.

The developed imaging system will not only be crucial in the understanding of microbubble oscillation, but also in the field of phase-change contrast agents. Although simulations have already illustrated the asymmetry in the phase-change process near a wall (Cho and Son 2018a, 2018b), the experimental recordings in publications typically provide a top view of the process (Sheeran et al. 2014; Shpak et al. 2014), missing the asymmetry introduced by the wall against which the droplets rest. In our study, the violent and asymmetric phase transition was captured by the two cameras from orthogonal views. Though the vaporization process seemed symmetric from the top, the side recording revealed a dome-shaped oscillation with a lower expansion perpendicularly and a smaller volume than a complete sphere to the resting surface. In the future, these recordings could provide insights into the natural frequency and dynamics of the vaporization process and resulting microbubbles, which is crucial to droplet-guided molecular imaging and drug delivery (Borden et al. 2020). Furthermore, the 3-D shape variation of the phase conversion and the following vibration could help in the validation of analytical and numerical models on ADV (Cho and Son 2018a, 2018b; Lacour et al. 2018), revealing the flow fields and the stresses that the vaporization process produces on the surrounding vessels.

In addition to the demonstrated experiments, the two coupled cameras are widely compatible with different experimental setups to elucidate different transient phenomena associated with ultrasound-mediated imaging and therapy. For example, the two-camera system has the potential to be easily combined with other imaging modalities, such as a confocal microscope (Beekers et al. 2019), to image the dynamic behavior of UCAs and the corresponding detailed cellular response. Furthermore, the two-camera system can be applied to ultrasound-mediated flow field measurements (Zou et al. 2019) and stress investigations (Palanca et al. 2015) together with microparticle image velocimetry and digital image correlation techniques. Another advantage of this system is that the two cameras can be triggered in a programmable way at a desired time point (in nanosecond resolution) and recording speed, which enables the ability to capture the instantaneous phenomenon that occurs after a period of insonification, for instance, microbubble coalescence (Postema et al. 2004; Segers et al. 2018b) and sonoporation recovery (Fan et al. 2014a, 2014b). This is a great improvement compared with other ultra-high-speed systems, such as the Brandaris 128 with which it is not possible to predict the start of an acquisition precisely because of the variability in the acceleration of the turbine. However, because of the pixel size of the camera, it will be difficult to obtain precise sizes of tiny microbubbles ($\leq$1 μm in diameter) at a magnification $\leq$100. There are also limitations to the two-camera system. For example, though the system supports continuous recording, the time between acquisitions is at least 7 s because of data saving and transmission. This time cost is relatively high in comparison to the 80 ms between recordings (maximally 33 recordings) for the Brandaris 128. Microbubble spectroscopy will therefore be challenging using the two-camera system. In addition, while the current orthogonal setup enables observation in two cross-sectional planes, it will be difficult to reconstruct a complex 3-D droplet vaporization or microbubble shape oscillation if more than two symmetric axes exist.

The results of the cross-correlation illustrate that the interleaving time is not perfectly 50 ns, as in the output exposure experiment this ranges from 48.3 to 48.6 ns and in the microbubble oscillation experiment this is 48.6 ns. These varied interleaving times were caused mainly by the transmission time consumed in the coupling cable. Furthermore, for the output exposure experiment, the interleaved time calculated was limited by the sampling rate of the oscilloscope (1 GS/s). However, the 1.3- to 1.7-ns deviation in the interleaving time is only 2.6%−3.4% of the 50-ns exposure time which overall has an insignificant influence on the 20-Mfps recording speed.

CONCLUSIONS

A novel, user-friendly and flexible ultra-high-speed imaging system with a recording speed up to 20 Mfps and 25.65-μs duration resulting in 512 frames was successfully developed by coupling two 10-Mfps commercially available cameras for interleaved imaging. Two verification experiments validated the 20-Mfps interleaving timing and reliability, which revealed ultrasound-activated microbubble dynamics. To the best of our knowledge, droplet vaporization was observed for the first time orthogonally at 10 Mfps. With this imaging system, detailed information can be obtained on the responses of contrast agents when exposed to ultrasound and advance the knowledge of the dynamics of UCAs and their interaction with living cells in an ultrasound field.

Acknowledgments—This work was funded by the European Research Council (ERC) under the European Union's Horizon 2020 Research and Innovation Program (Grant Agreement 805308). The authors thank Bram Meijlink (Erasmus MC) for microbubble production, Michiel Manten (Erasmus MC) for designing and manufacturing the orthogonal apparatus and Hendrik J. Vos (Erasmus MC) for the fruitful discussions on the orthogonal experiments.

Conflict of interest disclosure—The authors declare no known conflicts of interest.

SUPPLEMENTARY MATERIALS

Supplementary material associated with this article can be found in the online version at doi:10.1016/j.ultrasmedbio.2022.08.020.

REFERENCES

Beekers I, Lattwein KR, Kouijzer JJP, Langeveld SAG, Vegter M, Beurskens R, Mastik F, Verduyn Lunel R, Verver E, van der Steen AFW, de Jong N, Kooiman K. Combined Confocal microscope and Brandaris 128 ultra-high-speed camera. Ultrasound Med Biol 2019;45:2575–2582.

Beekers I, Vegter M, Lattwein KR, Mastik F, Beurskens R, van der Steen AFW, de Jong N, Verweij MD, Kooiman K. Opening of endothelial cell-cell contacts due to sonoporation. J Control Release 2020;322:426–438.

Bloch SH, Wan M, Dayton PA, Ferrara KW. Optical observation of lipid- and polymer-shelled ultrasound microbubble contrast agents. Appl Phys Lett 2004;84:631–633.

Borden MA, Shakya G, Upadhyay A, Song KH. Acoustic nanodrops for biomedical applications. Curr Opin Colloid Interface Sci 2020;50 101383.

Carlier B, Heymans SV, Nooijens S, Toumia Y, Ingram M, Paradossi G, D'Agostino E, Himmelreich U, D'Hooge J, Van Den Abeele K, Sterpin E. Proton range verification with ultrasound imaging using injectable radiation sensitive nanodroplets: A feasibility study. Phys Med Biol 2020;65 065013.

Chen H, Brayman AA, Kreider W, Bailey MR, Matula TJ. Observations of translation and jetting of ultrasound-activated microbubbles in mesenteric microvessels. Ultrasound Med Biol 2011a;37:2139–2148.

Chen H, Kreider W, Brayman AA, Bailey MR, Matula TJ. Blood vessel deformations on microsecond time scales by ultrasonic cavitation. Phys Rev Lett 2011b;106 034301.

Chen X, Wang J, Versluis M, de Jong N, Villanueva FS. Ultra-fast bright field and fluorescence imaging of the dynamics of micrometer-sized objects. Rev Sci Instrum 2013;84 063701.

Chin CT, Lancée C, Borsboom J, Mastik F, Frijlink ME, de Jong N, Versluis M, Brandaris Lohse D. 128: A digital 25 million frames per second camera with 128 highly sensitive frames. Rev Sci Instrum 2003;74:5026–5034.

Cho S, Son G. A level-set method for bubble growth in acoustic droplet vaporization. Int Commun Heat Mass Transfer 2018a;93:83–92.

Cho S, Son G. Numerical simulation of acoustic droplet vaporization near a wall. International Commun Heat Mass Transfer 2018b;99:7–17.

Christensen-Jeffries K, Couture O, Dayton PA, Eldar YC, Hynynen K, Kiessling F, O'Reilly M, Pinton GF, Schmitz G, Tang MX, Tanter M, van Sloun RJG. Super-resolution ultrasound imaging. Ultrasound Med Biol 2020;46:865–891.

Cleve S, Inserra C, Prentice P. Contrast Agent Microbubble Jetting during Initial Interaction with 200-kHz focused ultrasound. Ultrasound Med Biol 2019;45:3075–3080.

Collado-Lara G, Heymans SV, Rovituso M, Carlier B, Toumia Y, Verweij M, Paradossi G, Sterpin E, Vos HJ, D'Hooge J, de Jong N, Van Den Abeele K, Daeichin V. Spatiotemporal distribution of nanodroplet vaporization in a proton beam using real-time ultrasound imaging for range verification. Ultrasound Med Biol 2022;48:149–156.

Dave MJ, Pandya TS, Stoddard D, Street J. Dynamic characterization of biocomposites under high strain rate compression loading with split Hopkinson pressure bar and digital image correlation technique. International Wood Products J 2018;9:115–121.

Deprez J, Lajoinie G, Engelen Y, De Smedt SC, Lentacker I. Opening doors with ultrasound and microbubbles: Beating biological barriers to promote drug delivery. Adv Drug Deliv Rev 2021;172:9–36.

Ding HC, Wang ZM, Li YF, Xu HM, Zuo CJ. Initial dynamic development of fuel spray analyzed by ultra high speed imaging. Fuel 2016;169:99–110.

Dollet B, van der Meer SM, Garbin V, de Jong N, Lohse D, Versluis M. Nonspherical oscillations of ultrasound contrast agent microbubbles. Ultrasound Med Biol 2008;34:1465–1473.

Faez T, Skachkov I, Versluis M, Kooiman K, de Jong N. In vivo characterization of ultrasound contrast agents: Microbubble spectroscopy in a chicken embryo. Ultrasound Med Biol 2012;38:1608–1617.

Fan Z, Chen D, Deng CX. Characterization of the dynamic activities of a population of microbubbles driven by pulsed ultrasound exposure in sonoporation. Ultrasound Med Biol 2014a;40:1260–1272.

Fan Z, Kumon RE, Deng CX. Mechanisms of microbubble-facilitated sonoporation for drug and gene delivery. Ther Deliv 2014;5:467–486.

Gelderblom EC, Vos HJ, Mastik F, Faez T, Luan Y, Kokhuis TJ, van der Steen AF, Lohse D, de Jong N, Versluis M. Brandaris 128 ultra-high-speed imaging facility: 10 years of operation, updates, and enhanced features. Rev Sci Instrum 2012;83 103706.

Goh BHT, Conneely M, Kneuper H, Palmer T, Klaseboer E, Khoo BC, Campbell P. High-speed imaging of ultrasound-mediated bacterial

biofilm disruption. In: Lacković I, Vlacić D, (eds). IFMBE Proceedings: Vol. 45. 6th European Conference of the International Federation for Medical and Biological Engineering. Cham: Springer; 2015. p. 533.
Guedra M, Inserra C, Mauger C, Gilles B. Experimental evidence of nonlinear mode coupling between spherical and nonspherical oscillations of microbubbles. Phys Rev E 2016;94 053115.
Hay TA, Ilinskii YA, Zabolotskaya EA, Hamilton MF. Model for the dynamics of a spherical bubble undergoing small shape oscillations between parallel soft elastic layers. J Acoust Soc Am 2013;134:1454–1462.
Helfield B. A review of phospholipid encapsulated ultrasound contrast agent microbubble physics. Ultrasound Med Biol 2019;45:282–300.
Helfield B, Chen X, Watkins SC, Villanueva FS. Biophysical insight into mechanisms of sonoporation. Proc Natl Acad Sci USA 2016;113:9983–9988.
Kee ALY, Teo BM. Biomedical applications of acoustically responsive phase shift nanodroplets: Current status and future directions. Ultrason Sonochem 2019;56:37–45.
Koch BML, Lo C, Li HY, Sano T, Ligda J, Hogan JD. Two-dimensional dynamic damage accumulation in engineered brittle materials. Eng Fracture Mech 2021;244 107539.
Kokhuis TJA, Garbin V, Kooiman K, Naaijkens BA, Juffermans LJM, Kamp O, Versluis M, van der Steen AFW, de Jong N. Probing microbubble adhesion using secondary acoustic radiation force. Proc IEEE Int Ultrason Symp 2011;947–950.
Kooiman K, Roovers S, Langeveld SAG, Kleven RT, Dewitte H, O'Reilly MA, Escoffre JM, Bouakaz A, Verweij MD, Hynynen K, Lentacker I, Stride E, Holland CK. Ultrasound-responsive cavitation nuclei for therapy and drug delivery. Ultrasound Med Biol 2020;46:1296–1325.
Kouijzer JJP, Lattwein KR, Beekers I, Langeveld SAG, Leon-Grooters M, Strub JM, Oliva E, Mislin GLA, de Jong N, van der Steen AFW, Klibanov AL, van Wamel WJB, Kooiman K. Vancomycin-decorated microbubbles as a theranostic agent for *Staphylococcus aureus* biofilms. Int J Pharm 2021;609 121154.
Kudo N. High-speed in situ observation system for sonoporation of cells with size- and position-controlled microbubbles. IEEE Trans Ultrason Ferroelectr Freq Control 2017;64:273–280.
Kuroda R, Tochigi Y, Miyauchi K, Takeda T, Sugo H, Shao F, Sugawa S. A 20 Mfps global shutter CMOS image sensor with improved light sensitivity and power consumption performances. ITE Trans Media Technol Appl 2016;4:149–154.
Lacour T, Guedra M, Valier-Brasier T, Coulouvrat F. A model for acoustic vaporization dynamics of a bubble/droplet system encapsulated within a hyperelastic shell. J Acoust Soc Am 2018;143:23.
Lajoinie G, Luan Y, Gelderblom E, Dollet B, Mastik F, Dewitte H, Lentacker I, de Jong N, Versluis M. Non-spherical oscillations drive the ultrasound-mediated release from targeted microbubbles. Commun Physics 2018;1:22.
Langeveld SAG, Beekers I, Collado-Lara G, van der Steen AFW, de Jong N, Kooiman K. The impact of lipid handling and phase distribution on the acoustic behavior of microbubbles. Pharmaceutics 2021;13:119.
Lazarus C, Pouliopoulos AN, Tinguely M, Garbin V, Choi JJ. Clustering dynamics of microbubbles exposed to low-pressure 1-MHz ultrasound. J Acoust Soc Am 2017;142:3135.
Lee JY, Crake C, Teo B, Carugo D, de Saint Victor M, Seth A, Stride E. Ultrasound-enhanced siRNA delivery using magnetic nanoparticle-loaded chitosan−deoxycholic acid nanodroplets. Adv Healthc Mater 2017;6 1601246.
Liu Y, Calvisi ML, Wang Q. Shape oscillation and stability of an encapsulated microbubble translating in an acoustic wave. J Acoust Soc Am 2018;144:2189.
Morton JA, Khavari M, Qin L, Maciejewska BM, Tyurnina AV, Grobert N, Eskin DG, Mi J, Porfyrakis K, Prentice P, Tzanakis I. New insights into sono-exfoliation mechanisms of graphite: In situ high-speed imaging studies and acoustic measurements. Mater Today 2021;49:10–22.
Mulvana H, Browning RJ, Luan Y, de Jong N, Tang MX, Eckersley RJ, Stride E. Characterization of contrast agent microbubbles for ultrasound imaging and therapy research. IEEE Trans Ultrason Ferroelectr Freq Control 2017;64:232–251.
Palanca M, Tozzi G, Cristofolini L. The use of digital image correlation in the biomechanical area: a review. Int Biomech 2015;3:1–21.
Postema M, Marmottant P, Lancee CT, Hilgenfeldt S, de Jong N. Ultrasound-induced microbubble coalescence. Ultrasound Med Biol 2004;30:1337–1344.
Prentice P, Cuschierp A, Dholakia K, Prausnitz M, Campbell P. Membrane disruption by optically controlled microbubble cavitation. Nat Phys 2005;1:107–110.
Rapoport N, Nam KH, Gupta R, Gao Z, Mohan P, Payne A, Todd N, Liu X, Kim T, Shea J, Scaife C, Parker DL, Jeong EK, Kennedy AM. Ultrasound-mediated tumor imaging and nanotherapy using drug loaded, block copolymer stabilized perfluorocarbon nanoemulsions. J Control Release 2011;153:4–15.
Segers T, Gaud E, Versluis M, Frinking P. High-precision acoustic measurements of the nonlinear dilatational elasticity of phospholipid coated monodisperse microbubbles. Soft Matter 2018a;14:9550–9561.
Segers T, Lassus A, Bussat P, Gaud E, Frinking P. Improved coalescence stability of monodisperse phospholipid-coated microbubbles formed by flow-focusing at elevated temperatures. Lab Chip 2018b;19:158–167.
Sheeran PS, Matsunaga TO, Dayton PA. Phase change events of volatile liquid perfluorocarbon contrast agents produce unique acoustic signatures. Phys Med Biol 2014;59:379–401.
Sheng D, Deng L, Li P, Wang Z, Zhang Q. Perfluorocarbon nanodroplets with deep tumor penetration and controlled drug delivery for ultrasound/fluorescence imaging guided breast cancer therapy. ACS Biomater Sci Eng 2021;7:605–616.
Shpak O, Verweij M, Vos HJ, de Jong N, Lohse D, Versluis M. Acoustic droplet vaporization is initiated by superharmonic focusing. Proc Natl Acad Sci USA 2014;111:1697–1702.
Sijl J, Gaud E, Frinking PJ, Arditi M, de Jong N, Lohse D, Versluis M. Acoustic characterization of single ultrasound contrast agent microbubbles. J Acoust Soc Am 2008;124:4091–4097.
Sirsi SR, Borden MA. State-of-the-art materials for ultrasound-triggered drug delivery. Adv Drug Deliv Rev 2014;72:3–14.
Song R, Zhang C, Teng F, Tu J, Guo X, Fan Z, Zheng Y, Zhang D. Cavitation-facilitated transmembrane permeability enhancement induced by acoustically vaporized nanodroplets. Ultrason Sonochem 2021;79 105790.
Sun Y, Kruse DE, Dayton PA, Ferrara KW. High-frequency dynamics of ultrasound contrast agents. IEEE Trans Ultrason Ferroelectr Freq Control 2005;52:1981–1991.
Thoroddsen ST, Etoh TG, Takehara K. High-speed imaging of drops and bubbles. Annu Rev Fluid Mech 2008;40:257–285.
Versluis M. High-speed imaging in fluids. Exp Fluids 2013;54:1458.
Versluis M, Goertz DE, Palanchon P, Heitman IL, van der Meer SM, Dollet B, de Jong N, Lohse D. Microbubble shape oscillations excited through ultrasonic parametric driving. Phys Rev E Stat Nonlin Soft Matter Phys 2010;82 026321.
Vos HJ, Dollet B, Versluis M, de Jong N. Nonspherical shape oscillations of coated microbubbles in contact with a wall. Ultrasound Med Biol 2011;37:935–948.
Wu Q, Mannaris C, May JP, Bau L, Polydorou A, Ferri S, Carugo D, Evans ND, Stride E. Investigation of the acoustic vaporization threshold of lipid-coated perfluorobutane nanodroplets using both high-speed optical imaging and acoustic methods. Ultrasound Med Biol 2021;47:1826–1843.
Xing HZ, Zhang QB, Braithwaite CH, Pan B, Zhao J. High-speed photography and digital optical measurement techniques for geomaterials: Fundamentals and applications. Rock Mech Rock Eng 2017;50:1611–1659.
Zevnik J, Dular M. Cavitation bubble interaction with a rigid spherical particle on a microscale. Ultrason Sonochem 2020;69 105252.
Zhou Y. Application of acoustic droplet vaporization in ultrasound therapy. J Ther Ultrasound 2015;3:20.
Zou P, Li M, Wang Z, Zhang G, Jin L, Pang Y, Du L, Duan Y, Liu Z, Shi Q. Micro-particle image velocimetry investigation of flow fields of SonoVue microbubbles mediated by ultrasound and their relationship with delivery. Front Pharmacol 2019;10:1651.